Rate-Limiting Step in the Low-Energy Unimolecular Decomposition Reaction of $Ni^{+\bullet}$Acetone into Ni^+CO + Ethane

S. Jason Dee, Vanessa A. Castleberry, Otsmar J. Villarroel, Ivanna E. Laboren, Sarah E. Frey, Daniel Ashley, and Darrin J. Bellert*

Department of Chemistry and Biochemistry, Baylor University, One Bear Place #97348,
Waco, Texas 76798-7348

Received: July 21, 2009; Revised Manuscript Received: September 30, 2009

Rate constants for the low-energy Ni^+-assisted C−C bond cleavage reaction of deuterium-labeled acetone have been acquired under jet-cooled conditions in the gas phase. The energies used to initiate the dissociative reactions of the precursor complex ion $Ni^+(d_6\text{-Ac})$ are well below that required to cleave C−C σ-bonds in isolated organic molecules. The rate constants are compared to those acquired previously for the lighter $Ni^+(h_6\text{-Ac})$ isotope and result in a substantial kinetic isotope effect ($k_H/k_D \sim 5.5$). Arguments are made that implicate isomerization leading to C−C bond coupling as the rate-limiting step (not C−C σ-bond activation) in the dissociative reaction.

Introduction

Understanding the detail associated with gas-phase, metal-initiated catalytic-styled reactions is of continuing interest.[1−8] To this end, computational chemistry can provide fine aspects of the reaction coordinate which connects reactants to products.[8−16] However, often only simple reactions can be studied at high levels of theory due to many reaction complexities and, thus, computational cost. Nonetheless, when the theoretical community offers quality calculations, it is the experimental chemists who must provide comparative results. Recently, the potential energy surface associated with the Ni^+ + acetone reaction was calculated using density functional theory (DFT).[16] Their results were compared with Bowers' experimental measurement of the product kinetic energy release distributions (KERDs) from the Ni^+ + acetone reaction.[17] The two techniques disagreed as to the identity of the rate-determining step along the reaction coordinate. Theory[16] suggests that the Ni^+-mediated methyl migration is the rate-limiting step while Bowers' group concluded that the initial C−C σ-bond activation is rate-limiting.[17] The authors of the KERDs study arrived at their conclusion because statistical phase space theory required a tight transition state to accurately reproduce the KERD. The authors justified the choice of a rate-limiting C−C σ-bond activation step through comparison with similar systems (primarily M^+−propane)[18−20] and qualitative calculations which agreed with the KERDs measurements.[17]

Our experimental technique supplies the cold precursor ion with sufficient energy to induce a dissociative reaction. We then monitor the precursor ion decay directly as it develops in time according to eq 1, where A_0 and k indicate the initial concentration and the reaction rate constant, respectively.

$$A_t = A_0 e^{-kt} \tag{1}$$

Previously, we had applied our experimental technique to the $Ni^+(h_6\text{-Ac})$ system where unimolecular first-order dissociation rate constants were measured over a range of internal energies.[21] This study focuses on the heavier, deuterium-labeled analog $Ni^+(d_6\text{-Ac})$ to ascertain the rate-limiting step through measurement of the kinetic isotope effect. As a result, we have obtained energy-specific rate constants ($k(E)$) for both the bond activation and the methyl isomerization processes. These have been determined through either direct measurement or through simulation of the precursor depletion waveform. We have measured a large kinetic isotope effect (k_H/k_D ratio) that clearly implicates methyl migration as the rate-limiting step in the reaction coordinate. Our results support the conclusions drawn from the DFT investigations.

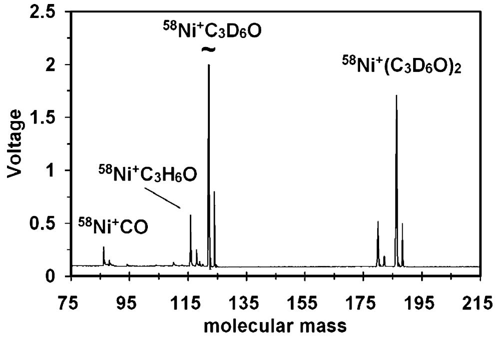

Figure 1. $Ni^+(d_6\text{-Ac})$ precursor ion time-of-flight mass spectrum.

Experimental Section

The instrument, and the method by which the data is analyzed, has been described previously.[21] Therefore, only a brief description is provided here. In general, a supersonic source chamber is connected to a custom time-of-flight mass spectrometer. Clusters generated in the source are mass-analyzed in the TOF. Source conditions are optimized to form the coldest ionic clusters possible. Under such cold conditions, Mach numbers as high as 70 are fairly easily realized for small ionic clusters. Figure 1 shows a routine mass spectrum acquired under optimal operational parameters.

More specifically, gaseous nickel cations are created through pulsed laser (248 nm) vaporization of a relatively pure (99%),

---

* Corresponding author. E-mail: Darrin_Bellert@baylor.edu. Fax: 254-710-4272.

10.1021/jp906912d

rotating nickel rod under high-vacuum conditions. A high-pressure, pulsed helium plume (doped with the vapor pressure of d_6-acetone) is timed to entrain the Ni^+ cations into the doped plume and cool the vaporization products through supersonic expansion into vacuum. Collisions between the acetone vapor and Ni^+ cations form the electrostatically bound title complex under jet-cooled conditions.

The supersonic expansion is skimmed twice and the beam approaches a Wiley−McLaren-type orthogonal accelerator (OA).[22] Along this approach, pulsed laser radiation counter-propagates to the molecular beam direction and is timed to intersect the clusters before pulsed extraction in the OA. Those ions that absorb the radiation and dissociate before entering the OA are accelerated along with all the other ions. These early dissociative fragment ions cannot be selectively transmitted through a hemispherical kinetic energy analyzer (sector). Thus, any early dissociation is not sampled. The precursor ions dissociating after orthogonal extraction, but before entering the sector, will yield fragment ions that are selectively transmitted to a microchannel plate detector located at the terminus of the sector. Monitoring only those fragment ions from the specific precursor ions dissociating between the OA and sector provide the signals acquired in this study.

The acquired signal arises from only those dissociative events occurring between the OA and sector, effectively integrating eq 1 between these limits. We define the following:

t_i: time when the ions just exit the OA and when the integration time begins

t_f: time just before the ions enter the electric field of the sector which marks the end of the integration time

Δt: $t_f - t_i$, or the time that the ions require to traverse the field free drift region of the TOF

τ: temporal displacement of the ions from the OA at the time the ions absorb dye laser radiation; this represents the decay time that is lost (not sampled) during the ions flight to the OA

During the experiment, the dissociation laser is timed to intersect the molecular beam at certain values of τ. Thus, the resulting exponential decay that occurs within the TOF is sampled and plotted as a single point, y_τ, given by

$$y_\tau = A_0 \int_{t_i}^{t_f} e^{-kt}\, dt = \frac{A_0}{k}(e^{-kt_i} - e^{-k(\Delta t + t_i)}) = \frac{A_0}{k}\left(e^{-kt_i}\left(1 - \frac{1}{e^{k\Delta t}}\right)\right) \quad (2)$$

Grouping the constants in eq 2 into α and substituting $t_i = \tau + 2.4$ μs (the time required for the $Ni^+(d_6\text{-Ac})$ ions to traverse the OA) results in eq 3, which is in analogous form to eq 1,

$$y_\tau = \left(\frac{\alpha}{e^{2.4k}}\right) A_0 e^{-k\tau} \quad (3)$$

where α is given in eq 4:

$$\alpha = \frac{1 - \frac{1}{e^{k\Delta t}}}{k} \quad (4)$$

Thus, a plot of y_τ versus τ should yield exponential decay like that predicted in eq 1; however, this parenthetical term in eq 3 will enhance the signal intensity acquired. Combining the α amplification with the rate constants observed in this study creates a data magnification of ~10−15 times.

SCHEME 1

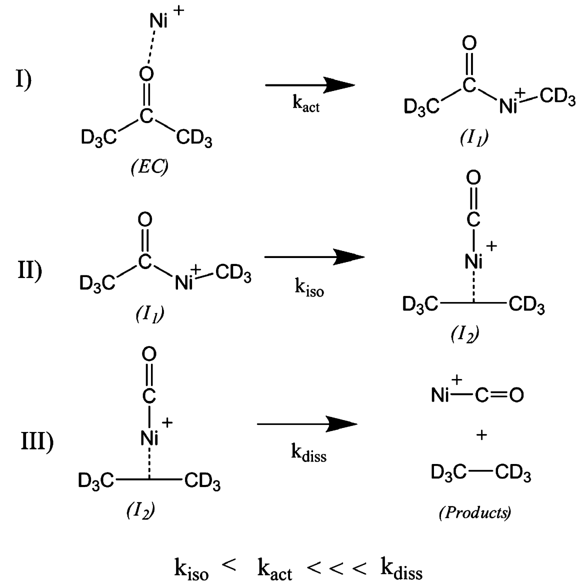

Results

Scheme 1 presents a series of elementary steps which shows the production of ethane and Ni^+CO resulting from the interaction of gaseous Ni^+ cations with acetone. Mechanisms similar to Scheme 1 have been presented before and were initially used to describe the interaction of gaseous Fe^+ with acetone.[23] Later, the same mechanism was applied to the reactions of gaseous Ni^+ and Co^+ with acetone.[17,24] Scheme 1 has been verified through DFT calculations.[16] It begins with the $Ni^+{-}OC(CD_3)_2$ dipole bound encounter complex, formed and cooled through a laser-driven supersonic expansion. After absorption of a visible laser photon, the complex has sufficient internal energy to induce chemical reaction and approaches intermediate 1 (I_1) through transition state 1. The first transition state (not shown) is a multicentered Ni^+ bound complex which places the Ni^+ cation in close proximity to a C−C σ-bond of acetone. The first intermediate, (I_1), represents the Ni^+-inserted complex and its formation is governed by the activation rate constant k_{act}. The second intermediate (I_2) along the reaction coordinate is an ethane molecule electrostatically bound to a Ni^+CO complex ion. This occurs as I_1 rearranges into I_2 through the second transition state. This process is controlled by the isomerization rate constant k_{iso}. The final step in the mechanism is the release of product and consequent formation of C_2D_6 and Ni^+CO, of which Ni^+CO was the only observed product.

The experiment conducted here monitors the rate of precursor ion depletion following the deposition of a known amount of energy into the cold precursor complex ion. The rate of precursor depletion is limited by the slowest step in Scheme 1. The final step (dissociation) does not involve bond activation or significant rearrangement and is therefore not rate-limiting (k_{diss} is assumed to be relatively large). Therefore, either C−C σ-bond activation or the Ni^+-mediated isomerization step is the rate-limiting step. To determine whether k_{act} or k_{iso} is smallest, the deuterium-labeled unimolecular decomposition of Ni^+−acetone ($Ni^+(d_6\text{-Ac})$) was monitored and compared with the previously studied h_6-Ac system.[21]

The central and lower panels of Figure 2 show the exponential decay of Ni^+(Ac) precursor ions into Ni^+CO + ethane. The

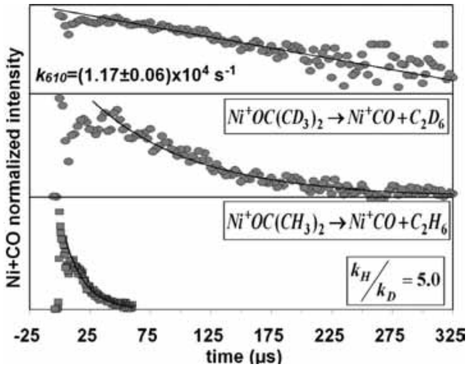

Figure 2. Bottom two panels plot the normalized signal intensity of the measured dissociative fragment (Ni^+CO) where the decomposition for each reaction is initiated by single-photon absorption (laser photon energy = 16 400 cm^{-1}). The bottom panel plots this for the Ni$^+$(h_6-Ac) precursor ion while the center panel shows this for Ni$^+$(d_6-Ac). The top panel plots the natural logarithm of the intensity vs time in the Ni$^+$(d_6-Ac) study. First-order decay constants are extracted from this treatment.

two panels represent the decay waveforms of the isotopic variants [Ni$^+$(d_6-Ac) and Ni$^+$(h_6-Ac)]. The waveforms result from the decomposition reaction initiated by single-photon absorption (energy = 16 400 cm^{-1}). Since the molecular ions are jet-cooled prior to laser interrogation, the photon energy represents the total amount of energy available to the complex. Therefore, the absorbed photon energy approximates the internal energy of the complex prior to photodissociation. Again, the photon energy that initiates the dissociative reaction is significantly less than that required to break C−C σ-bonds typical of isolated organic molecules.

The time axis of Figure 2 is the temporal displacement of the precursor ions relative to the OA. This time also represents when the pulsed dye laser radiation intersects the cold precursor ions to supply the activation energy, initiating the dissociative reaction. At 0 μs, the laser radiation intersects the molecular beam within the OA. This encounter occurs nanoseconds prior to charging the acceleration grid and initiating orthogonal extraction. At all negative values of time, the ion beam turns 90° before the laser is triggered to fire. Signals at negative time are therefore due to collisional dissociation of the precursor ions within the field free flight of the TOF. At all positive values of time, the laser is triggered to fire and intersects the molecular beam in the expanse between the pulsed valve and the OA. The fragments that form prior to extraction cannot be differentiated from the precursor ion beam by selective transmission through the hemispherical sector. Only those excited precursor ions decaying after orthogonal extraction, but before entering the sector, will produce fragment ions that can be separated (and thus selectively detected) from the ion beam via sector transmission. Therefore, as the time axis increases, the relative number of fragments detected decrease since the excited precursors have more time to decay into undetectable fragments prior to pulsed extraction.

Additionally, dissociative fragments are monitored for all molecular decay which occurs during the entire field free drift time in the TOF. Thus, the signals acquired result from integrating the unimolecular decay waveform between two distinct times: the time at which the excited precursor ions just exit the OA (t_i) and the time just before entrance into the sector (t_f). Integrating the waveform provides more signal than otherwise would be acquired. However, under certain conditions, the integration may result in unexpectedly shaped decay curves. The early decay in the central panel of Figure 2 is distorted by a long 31 μs induction period (fragments are not observed for the first 31 μs following single-photon absorption). This induction period, t_{ind}, represents a time equivalent nearly as long as the TOF which is part of the reason for this distortion. Additionally, dissociation contamination from fast two-photon absorption events may be present at early times (first 5 μs). The final 200 μs of the waveform shows first-order exponential decay; moreover, the natural logarithm of this portion is fit to a straight line as is shown in the top panel of Figure 2. A single rate constant, $k(E = 16\,400$ cm^{-1}) = 11 700 ± 600 s^{-1} (see Table 1) is extracted from linear regression analysis and represents the rate-determining step (either k_{act} or k_{iso}) from Scheme 1. The fit parameters are used to construct the solid decay curve drawn through the data points of the central panel.

The lower panels of Figure 2 compare the unimolecular decay waveforms between $Ni^+OC(CH_3)_2 \rightarrow Ni^+CO + C_2H_6$ (bottom panel) and the deuterium-labeled isotope, $Ni^+OC(CD_3)_2 \rightarrow Ni^+CO + C_2D_6$ (middle panel). Both waveforms were acquired at comparable instrumental settings and the same laser energy (16 400 cm^{-1}) was used to initiate each reaction. The striking feature is the obvious difference in reaction rates between the two isotopes. The heavier, deuterium-labeled acetone isotope requires significantly longer times to produce Ni^+CO dissociative fragments. The rate constants extracted from these analyses are for the rate-limiting step in Scheme 1. The rate-limiting rate constant in the low-energy activation of acetone by gaseous Ni$^+$ is ~5 times smaller for the heavier, deuterium-labeled acetone isotope at the reaction initiation energy used in this study. Table 1 lists the rate constants measured here and those found earlier for the $Ni^+OC(CH_3)_2 \rightarrow Ni^+CO + C_2H_6$ reaction.[21]

To validate the decay data acquired at 16 400 cm^{-1}, analogous measurements were conducted using another laser energy. The central panel of Figure 3 shows the unimolecular decay of Ni$^+$(d_6-Ac) precursor ions into Ni^+CO and C_2D_6 resulting from the absorption of 18 000 cm^{-1} of laser photon energy. Consistent with Figure 2, the decay curve shows somewhat unexpected behavior at early times, which is due to the long induction period before product Ni^+CO fragments are produced. (Although the waveforms are distorted, they can be satisfactorily reproduced through simulation, as shown below.) The well-behaved exponential profile from ~25−200 μs is fit to a straight line in the top panel of Figure 3 and the rate constant is extracted from linear regression analysis. The parameters from the fit are used to generate the solid curve through the data points in the central panel. The quality of the fit indicates that the later portion of the decay curve is well described by a single exponential with a decay constant of $k(E = 18\,000$ cm^{-1}) = 16 000 ± 800 s^{-1} (see Table 1).

Furthermore, Figure 3 compares the unimolecular decay waveforms between the precursors Ni$^+$(d_6-Ac) and Ni$^+$(h_6-Ac) (bottom panel) acquired at a photon energy of 18 000 cm^{-1}. As before, there is a striking difference observed between the decay rates. The rate constant describing the decay of the lighter Ni$^+$(h_6-Ac) is roughly 6 times larger than that for the heavier, deuterium-labeled isotope.

Waveform Simulations

As indicated in our earlier study,[21] there are two kinetically important steps along the reaction coordinate controlling the reaction dynamics. These are the formation of I_1 (k_{act}) and I_2 (k_{iso}) in Scheme 1. Our technique measures the rate-limiting rate constant directly. Therefore, the rate constants extracted from the long exponential profiled in Figures 2 and 3 are either k_{act} or k_{iso}. To approximate the rate constant value which is not

TABLE 1: Kinetic Parameters for the Low-Energy Reaction of h_6- and d_6-Acetone with Gaseous Ni^+

	$Ni^+(h_6\text{-Ac}) \rightarrow Ni^+CO + C_2H_6$			$Ni^+(d_6\text{-Ac}) \rightarrow Ni^+CO + C_2D_6$		
internalenergy(cm^{-1})	$k_{iso}(E)^a$ ($\times 10^4$) s^{-1}	$k_{act}(E)^b$ ($\times 10^4$) s^{-1}	$t_{ind}{}^b$ (μs)	$k_{iso}(E)^a$ ($\times 10^4$) s^{-1}	$k_{act}(E)^b$ ($\times 10^4$) s^{-1}	$t_{ind}{}^b$ (μs)
18 800	11.3 ± 0.5					
18 000	9.68 ± 0.03	21.0	7	1.60 ± 0.08	12.5	19
17 700	9.27 ± 0.03					
16 700	5.90 ± 0.02					
16 400	5.90 ± 0.02	13.1	11	1.17 ± 0.06	6.7	31
16 100	5.80 ± 0.03					
15 600	5.50 ± 0.03					

[a] Measured directly. [b] Determined through simulation. Values without error limits should be assumed accurate to ±10%.

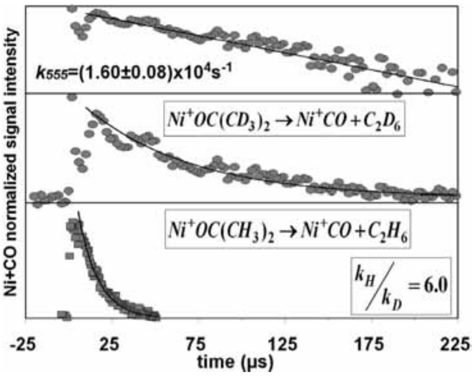

Figure 3. Same comparative kinetic study as Figure 2, except the reaction is initiated with a photon of energy = 18 000 cm^{-1}.

directly measured by this technique, and to quantify the induction times evident in the precursor decay profiles, software was developed to simulate the precursor decay waveform under instrumental conditions.

Scheme 1 is a mechanism of consecutive steps to produce Ni^+CO and ethane from the precursor Ni^+(Ac). The solutions to the differential rate equations that govern precursor loss and fragment production have been solved for this type of system by Harcourt and others.[25,26] Following their treatment, the time variations in the concentrations of $(Ni^+Ac)_t$, the first intermediate $(I_1)_t$ and product $(Ni^+CO)_t$ can be derived:

$$(Ni^+Ac)_t = (Ni^+Ac)_0 e^{-k_1 t} \tag{5}$$

$$(I_1)_t = (Ni^+Ac)_0 \frac{k_1}{k_2 - k_1}(e^{-k_1 t} - e^{-k_2 t}) \tag{6}$$

$$(Ni^+CO)_t = \frac{(Ni^+Ac)_0}{k_2 - k_1}[k_2(1 - e^{-k_1 t}) - k_1(1 - e^{-k_2 t})] \tag{7}$$

where k_1 and k_2 are general rate constants representing the two slower steps in Scheme 1. These rate equations represent a model, which when programmed, result in software that produces three waveforms: precursor depletion (eq 5), the buildup and depletion of the first intermediate (eq 6), and fragment production (eq 7). The program generates a fourth waveform by integrating fragment production under instrumental conditions, thus simulating observation. The simulation is not dependent upon the assignment of the k_1 or k_2 as rate-limiting. To operate the software, one of the rate constants is input as the fixed value determined through regression analysis. The remaining two input parameters ($(Ni^+Ac)_0$, k_1 or k_2) are manually adjusted until the contour of the simulated waveform overlays the experimental waveform. However, under the constraints of eqs 5–7, no combination of the input values could be found to provide adequate simulation of the observed waveform. It appears that direct application of the rate equations (eqs 5–7) is incapable of modeling the early portions of the decay.

Through observation, the character of the depletion waveforms indicates that fragment ions are not immediately produced, as indicated by eq 7. Therefore, to improve the model, an induction period is implemented that delays fragment production. The assumption is that this delay correlates with the time of maximum intermediate production; thus, fragments are not observed in sufficient quantity until the intermediate has reached maximum concentration. The program is modified to incorporate this induction period and this value is determined by setting the first derivative of eq 6 equal to 0 and solving for the time. This time, which equates with the maximum intermediate concentration, is provided by eq 8,

$$t_{ind} = \frac{\ln\left(\frac{k_2}{k_1}\right)}{k_2 - k_1} \tag{8}$$

It should be noted that incorporating the induction time in such fashion does not provide any additional adjustable parameters to the model. Application of the improved model adequately simulates the experimental waveforms as shown in Figures 4–7. Again, one rate constant (k_1 or k_2) is fixed by the value measured directly and the remaining two parameters (the initial concentration and the remaining rate constant) are adjusted until agreement between simulation and experiment is visually confirmed.

The top panels of Figures 4 and 5 show the simulated (solid curve) superimposed upon the observed (points) in the $Ni^+(h_6$-Ac) depletion waveforms. The lower panels display the precursor and intermediate waveforms generated from eqs 5 and 6. The fragment production waveform is from eq 7; however, this waveform is delayed by the induction period which correlates with maximum intermediate concentration. The rate constants used to generate the simulated waveform in Figure 4 are $k_1 = 21.0 \times 10^4$ s^{-1} and $k_2 = 9.68 \times 10^4$ s^{-1}, where k_2 was held constant at the value acquired through regression analysis.[21] The rate constants (labeled as k_{act} and k_{iso}), and also the induction times, can be seen in Table 1.

The observed $Ni^+(d_6$-Ac) depletion waveforms are shown in the top traces of Figures 6 and 7. The solid lines are simulated using the same modeling software. Again, fragment production (bottom trace) must be delayed until the intermediate has reached maximal concentration to adequately reproduce the early portions of the decay waveform. The induction period and relatively small rate constants are responsible for the apparent

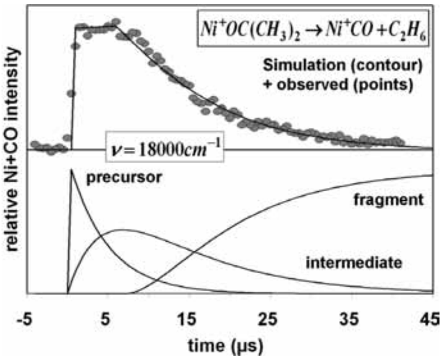

Figure 4. (Top panel): The Ni^+(h_6-Ac) decay waveform shown with simulation. The photon energy used to initiate the decomposition reaction is 18 000 cm^{-1}. (Bottom panel): The three waveforms showing precursor depletion, intermediate production followed by depletion, and fragment production (delayed by the induction period which correlates with the maximum in the intermediate waveform). Fragment production was integrated under instrumental conditions to generate the simulation in the top panel.

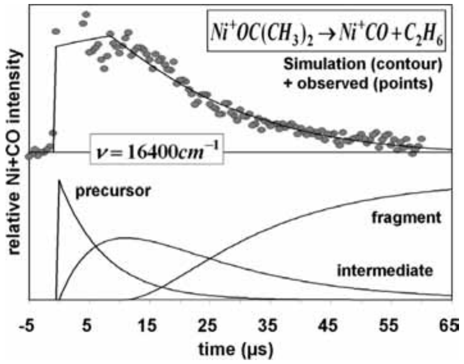

Figure 5. Same type of kinetics simulations as Figure 4, except the reaction was initiated with a photon of 16 400 cm^{-1}.

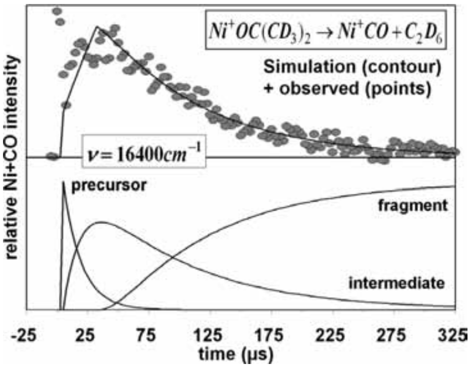

Figure 6. Same type of kinetics simulations shown in Figure 5 except for the unimolecular decay of the Ni^+(d_6-Ac) precursor ion.

cusp in the simulated and observed precursor ion decay waveforms in the top panels of Figures 6 and 7. The rate constants used in the simulation, and also the resulting induction periods, are shown in Table 1.

To summarize, the findings presented here are comparable to our earlier study of the decomposition reaction: Ni^+(h_6-Ac) → $Ni^+CO + C_2H_6$.[21] The rate constants decrease with decreasing precursor ion internal energy whereas the induction times increase with decreasing amounts of energy. The difference in this study is the kinetic isotope effect, which is now quantified. The average k_H/k_D ratio for one set of rate constants is ~5.5 while the average ratio for the other rate constant set is ~1.8. The results presented in this study, and also the lighter isotopic analog, are summarized in Table 1.

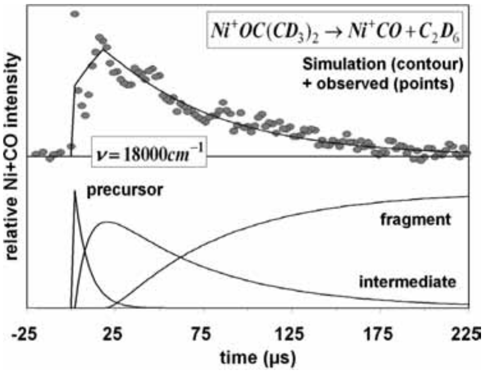

Figure 7. Same type of kinetics simulations shown in Figure 4 except for the unimolecular decay of the Ni^+(d_6-Ac) precursor ion.

Discussion

A. Electronic Transition and Deposition of Energy. The electronic transition and deposition of energy resulting in the decomposition reaction Ni^+(h_6-Ac) → $Ni^+CO + C_2H_6$ has been presented earlier;[21] therefore, only a brief overview will be given here. The ground electronic state of the Ni^+(Ac) complex ion is likely formed from the electrostatic attraction between the ground-state Ni^+ cation [$^2D(3d^9)$[27]] bound to the dipole moment (2.84 D)[28] of neutral acetone. The bonding is likely electrostatic as the ion-dipole attractive potential, at the $Ni^+{-}OC(CH_3)_2$ distance predicted by theory,[16] is 19 600 cm^{-1}. The bond energy of Ni^+(h_6-Ac) has been calculated[16] as 20 300 cm^{-1}. The energy required to ionize atomic nickel is ~16 500 cm^{-1}, less than that required to ionize acetone.[27] This large difference in ionization energy suggests that the charge in the complex is localized on the nickel.

Upon laser irradiation, the Ni^+(Ac) complex ion absorbs a visible photon and is promoted to an electronically excited state. The Ni^+ cation is the chromophore, as electronic transitions in acetone occur only in the UV.[29,30] The lowest lying, excited electronic state of Ni^+ is a $^4F(3d^84s)$ with lowest energy spin-orbit component ($J = 9/2$) lying 8393.9 cm^{-1} above the Ni^+ ^2D ground state. Electronic transition to this ^4F manifold of states initiates the dissociative chemical reactions observed in this study. This Ni^+-centered electronic transition $\{^4F(3d^84s) \leftarrow {}^2D(3d^9)\}$ is both spin- and parity-forbidden. The prepared, excited quartet electronic state of Ni^+(Ac) is metastable; the absorbed photon energy is insufficient to cause direct dissociation into Ni^+ and acetone fragments (the energy of the prepared state is below the adiabatic bond energy of the complex), and coupling to the ground state through photon emission is optically forbidden. Rather, the excited quartet state intersystem crosses to the doublet electronic state and deposits the energy of the electronic transition (or the photon energy) into the high vibrational levels of the ground state. Energy deposition in these high vibrational states provides the activation energy for unimolecular dissociation into fragments. Additionally, the deposited photon energy is likely localized in the cluster vibrational modes (those involving motion between the Ni^+ and neutral acetone) of the molecule. The cluster modes may inefficiently couple to the vibrational modes of the acetone molecule. The net effect of this coupling is the localization of energy and provision of sufficient motion to allow Ni^+ activation of the C−C σ-bond in acetone.

B. Rate-Limiting Step in the Unimolecular Dissociation of Ni^+(Ac). There are two kinetically important steps in the dissociative reaction between Ni^+ and acetone. The rate-limiting rate constants in the unimolecular decomposition for both the

$Ni^+(h_6\text{-Ac})$ and the deuterium-labeled $Ni^+(d_6\text{-Ac})$ have been measured directly. The kinetic isotope effect (k_H/k_D) associated with the rate-limiting step has an average value of ~5.5. The rate constants associated with the other kinetically important step have been approximated through simulation generated from models based on the rate equations governing consecutive reactions. The kinetic model provides rate constants which have an average ratio of ~1.8 (see Table 1). Since the rate-limiting step presents a kinetic isotope effect with a larger ratio magnitude, the rate-limiting step must involve the larger amplitude motion of the isotopically labeled species. In this study, the only candidates for the rate-limiting step are either C−C bond activation or methyl isomerization, as both have been previously implicated.[16,17] It is clear from Scheme 1 that isomerization of the methyl group involves the greater amplitude motion and is therefore responsible for the large kinetic isotope effect measured here for the rate-limiting step. We therefore conclude that methyl isomerization is the rate-limiting step along the $Ni^+(Ac)$ reaction coordinate. However, to validate this conclusion, we turn to the DFT calculations of Chen et al.[16]

From the minimized geometries of the DFT[16] calculated reaction coordinate, in order for the complex to progress from the initial encounter complex (EC) to I_1, the Ni^+ cation moves relative to a nearly stationary acetone molecule. The motion expressed by the acetone molecule is a 40% lengthening of the $C{-}CH_3$ σ-bond as the cation approaches. Once this first transition state is formed, the Ni^+ inserts exoergically into the acetone C−C bond and I_1 represents a local minimum along the reaction coordinate. The first intermediate has C_s symmetry with the Ni^+ cation, oxygen, and the two previously bonded carbons in a common plane. The $C{-}Ni^+{-}C$ bond angle is 113° with the remaining methyl group tilted away from the Ni^+. This intermediate isomerizes to form the second transition state, which involves methyl migration to the Ni^+ center. The migration path can be visualized as an $O{=}C{-}CH_3$ rotation about the $Ni^+{-}C$ bond axis until the $Ni^+{-}C{-}O$ bond angle is nearly linear. As the methyl swings to the opposite side of the molecule, the remaining $C{-}CH_3$ σ-bond lengthens nearly 40% and the methyl carbon bonds to the Ni^+ center forming the tricoordinated cation. Calculation indicates that the formation of this transition state involves significant motion of the methyl group and lies 12.9 kcal/mol above the C−C bond activation transition state.[16]

Therefore, the DFT calculated reaction coordinate places the isomerization of the methyl group as the most energetically demanding transition state, in complete agreement with our measurements. Additionally, calculation places the C−C bond activation transition state 40.5 kcal/mol above the encounter complex. Such a large activation energy indicates that this step should be kinetically important, again in agreement with our measurements.

The most probable reason as to why the formation of the tricoordinated cation is rate-limiting is due to the inability of Ni^+ to form three simultaneous covalent interactions. The ground electronic state of the Ni^+ cation is a $^2D(3d^9)$. To form the covalent bonds in the inserted complex (I_1), the cation likely promotes to the $^4F(3d^84s)$ configuration which now has two unpaired electrons. The electronic promotion cost (~8400 cm^{-1}) is offset by the bonding to the methyl and carbonyl carbons. The formation of three covalent bonds necessitates one additional unpaired Ni^+ electron, which is unlikely as the energy promotion costs would be prohibitive.

C. Induction Periods in the Dissociation of $Ni^+(Ac)$. Previously, rate constants ($k(E)$) associated with the unimolecular decomposition of $Ni^+(h_6\text{-Ac})$ were measured.[21] Those early results indicated the necessity to include an induction period to describe the precursor ion decay waveform at low amounts of internal excitation. At that time, the rate-limiting step was ascribed to one of the two processes, activation or isomerization, and the induction period was associated with the other. These early results, however, could not identify which process was rate-limiting.

The current studies on the deuterium-labeled $Ni^+(d_6\text{-Ac})$ analog clarify those initial results. The rate-limiting step is the isomerization of the first intermediate as the methyl group migrates to the cation. The rate constants which are measured directly here (and which have been measured for the $Ni^+(h_6\text{-Ac})$ system)[21] are $k_{iso}(E)$. The induction periods which must be invoked to describe the observed decay waveforms are associated with the activation of the C−C σ-bond and consequent formation of the first intermediate. Essentially, the Ni^+CO product ion cannot be observed until a sufficient quantity of I_1 is produced. The time required to produce this quantity is the induction time. Simulations indicate that the induction time correlates with maximal production of the first intermediate.

Conclusions

The rate-limiting step in the low-energy reaction to form neutral ethane gas and Ni^+CO from the electrostatic bound $Ni^+(Ac)$ complex is the isomerization of the methyl group leading to C−C bond coupling. This step follows the activation of the C−C σ-bond. This is concluded by measuring the unimolecular decomposition rate constants for both the $Ni^+(h_6\text{-Ac})$ and the deuterium-labeled $Ni^+(d_6\text{-Ac})$ species. The results showed that deuterium labeling affected both the activation and the isomerization step leading to the production of Ni^+CO. Thus, both are kinetically important processes in the Ni^+-assisted dissociation of acetone into ethane and Ni^+CO. The rate constants associated with bond activation (determined through kinetic simulation) yielded a kinetic isotope effect of nearly 2. The rate-limiting rate constants directly measured by this technique resulted in an averaged ratio of ~5.5. Logically, this larger effect results from methide isomerization, as this step necessitates a larger amplitude motion from the isotopically labeled methyl group.

Acknowledgment. We gratefully acknowledge research support from the ACS Petroleum Research Fund (44393-G6). Additionally, funds from the Baylor University Research Committee and the Vice Provost for Research supported this study. Finally, we thank the reviewers of this article for their helpful recommendations.

References and Notes

(1) Freiser, B. S. *J. Mass Spectrom.* **1996**, *31*, 703.

(2) Operti, L.; Rabezzana, R. *Mass Spectrom. Rev.* **2006**, *25*, 483.

(3) Allison, J. In *Progress in Inorganic Chemistry*; Lippard, S. J., Ed.; Wiley: New York, 1986; Vol. 34.

(4) Buckner, S. W.; Freiser, B. S. In *Gas Phase Inorganic Chemistry*; Russell, D. H., Ed.; Plenum Press: New York, 1989.

(5) Dunbar, R. C. In *Gas Phase Inorganic Chemistry*; Russell, D. H., Ed.; Plenum Press: New York, 1989.

(6) Beauchamp, J. L.; Van Koppen, P. A. M. *NATO ASI Ser., Ser. C.* **1992**, *367*, 287.

(7) Hettich, R. L.; Freiser, B. S. Gas-Phase Photodissociation of Transition Metal Ion Complexes and Clusters. In *Fourier Transform Mass Spectrometry*; Buchanan, M. V., Ed.; ACS Symposium Series 359; American Chemical Society: Washington, DC, 1987.

(8) Baer, T.; Hase, W. L. *Unimolecular Reaction Dynamics: Theory and Experiments*; Oxford University Press: New York, 1996.

(9) Barnes, L. A.; Rosi, M.; Bauschlicher, C. W., Jr. *J. Chem. Phys.* **1990**, *93*, 609.

(10) Blomberg, M.; Brandemark, U.; Johansson, J.; Siegbahn, P.; Wennerberg, J. *J. Chem. Phys.* **1988**, *88*, 4324.

(11) Bauschlicher, C. W., Jr.; Langhoff, S. R.; Partridge, H.; Barnes, L. A. *J. Chem. Phys.* **1989**, *91*, 2399.

(12) Zhang, D.-J.; Liu, C.-B.; Liu, Y.-J.; Hu, H.-Q. *Chin. J. Chem.* **2002**, *20*, 220.

(13) Reichert, E. L.; Weisshaar, J. C. *J. Phys. Chem. A* **2002**, *106*, 5563.

(14) Liu, F.; Zhang, X.-G.; Armentrout, P. B. *Phys. Chem. Chem. Phys.* **2005**, *7*, 1054.

(15) Yi, S. S.; Blomberg, M. R. A.; Siegbahn, P. E. M.; Weisshaar, J. C. *J. Phys. Chem. A* **1998**, *102*, 395.

(16) Chen, X.; Guo, W.; Zhao, L.; Fu, Q. *Chem. Phys. Lett.* **2006**, *432*, 27.

(17) Carpenter, C. J.; van Koppen, P. A. M.; Bowers, M. T. *J. Am. Chem. Soc.* **1995**, *117*, 10976.

(18) Hanratty, M. A.; Beauchamp, J. L.; Illies, A. J.; van Koppen, P. A. M.; Bowers, M. T. *J. Am. Chem. Soc.* **1988**, *110*, 1.

(19) Van Koppen, P. A. M.; Bowers, M. T.; Fisher, E. R.; Armentrout, P. B. *J. Am. Chem. Soc.* **1994**, *116*, 3780.

(20) Noll, R. J.; Yi, S. S.; Weishaar, J. C. *J. Phys. Chem. A* **1998**, *102*, 386.

(21) Castleberry, V. A.; Dee, S. J.; Villarroel, O. J.; Laboren, I. E.; Frey, S. E.; Bellert, D. J. *J. Phys. Chem. A* **2009**, *113*, 10417.

(22) Wiley, W. C.; McLaren, I. H. *Rev. Sci. Instrum.* **1955**, *26*, 1150.

(23) Burnier, R. C.; Byrd, G. D.; Freiser, B. S. *J. Am. Chem. Soc.* **1981**, *103*, 4360.

(24) Halle, L. F.; Crowe, W. E.; Armentrout, P. B.; Beauchamp, J. L. *Organometallics* **1984**, *3*, 1694.

(25) Laidler, K. J. *Chemical Kinetics, 3rd Ed.*; Harper and Row: New York, 1987.

(26) Harcourt, A. V.; Esson, W. *Proc. R. Soc. London* **1865**, *14*, 470.

(27) Shimanouchi, T. *Tables of Molecular Vibrational Frequencies Consolidated Volume I*; National Bureau of Standards: Washington, DC, 1972; pp 1−160.

(28) *CRC Handbook of Chemistry and Physic*, 71st ed.; CRC Press: Boca Raton, FL, 1990−1991.

(29) Haas, Y. *Photochem. Photobiol. Sci.* **2004**, *3*, 6.

(30) Goncharov, V.; Herath, N.; Suits, A. G. *J. Phys. Chem. A* **2008**, *112*, 9423.

JP906912D